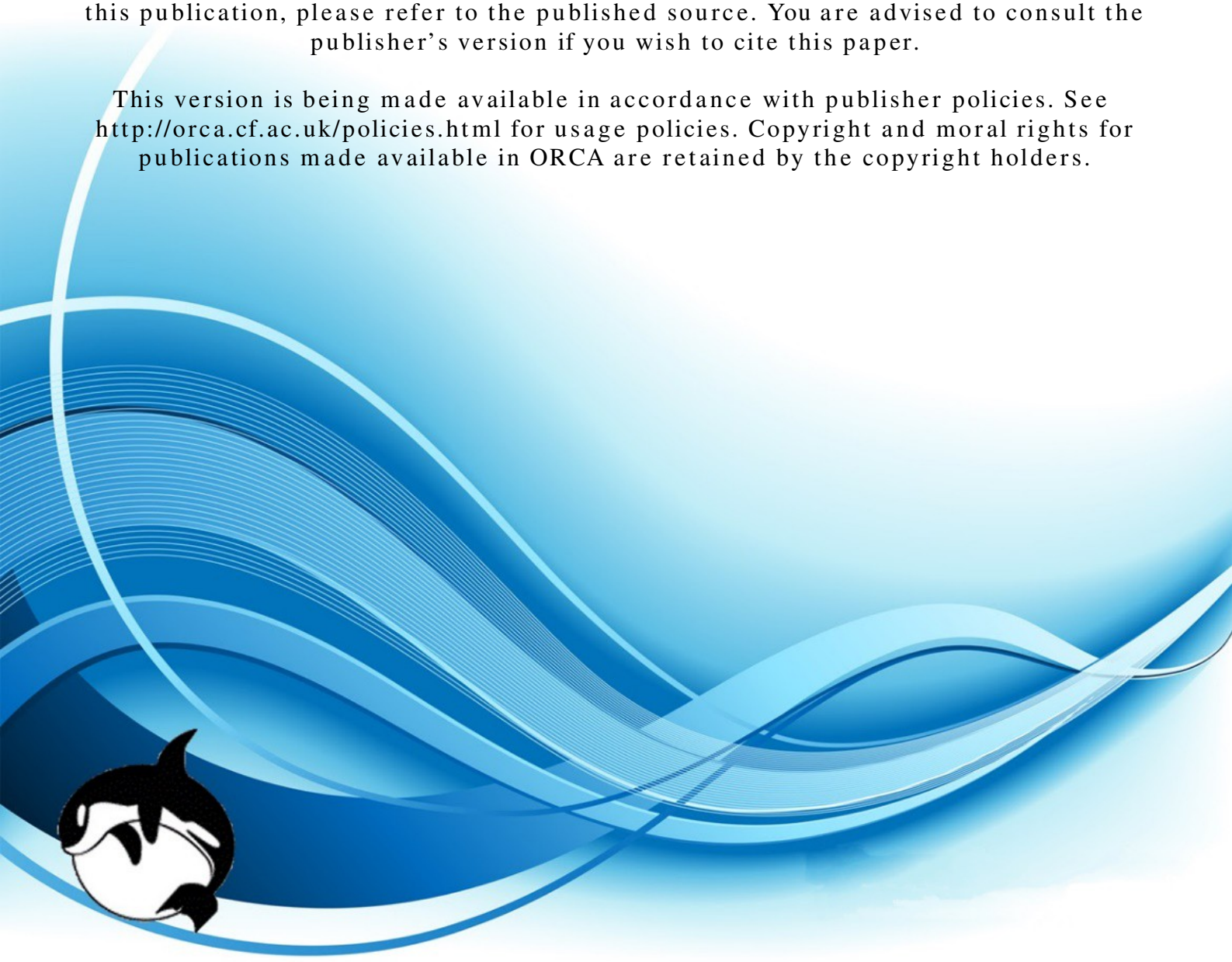

Photovoltaic modulating retroreflectors for low power consumption free space optical communication systems

Benjamin C. Maglio, Crisanto Quintana, Yoann Thueux, and Peter M. Smowton

***Abstract*—an InGaAs-InAsP-GaInP asymmetric stepped quantum well structure is proposed for unbiased detection and subsequent modulation of an incident continuous wave optical signal for application in compact, retroreflective, free-space optical communication platforms. Such operation drastically reduces onboard power consumption in large-area, pixelated arrays by driving only optically activated pixels. A modelling routine involving calculations of band structure, fraction of light absorbed, and responsivity have been used to analyse structures exhibiting an asymmetric quantum confined Stark effect. The proposed structure, compared with devices following similar modelling approaches, is predicted to exhibit an unbiased responsivity of 0.004 A/W enabling single pixel detection prior to triggering modulation. The calculated photocurrent of 4μA offers adequate signal to noise against dark current when operated in a photovoltaic mode. Furthermore, the strong blueshift in the ground state transition energy calculated for the applied field results in extinction ratios in excess of 4dB for the modulated signal. These findings suggest performance enhancements at a fraction of current onboard power consumption in modulating retroreflectors for compact, free-space optical communication platforms.**

***Index Terms*—III-V compound semiconductors, free space optics, modulating retroreflector, quantum confined Stark effect, quantum wells, optical communications, Internet of Things**

I. INTRODUCTION

FREE space optics (FSO) is a secure, high bandwidth method of wireless communication without spectrum licensing requirements [1]. These advantages over radio frequencies can be realised for remote applications with direct lines of sight such as plane to plane or intersatellite communication links [2]. Additionally, they provide Low Probability of Intercept/ Detection, which is desirable in defense applications. Traditionally, FSO systems use two laser transceivers to implement bidirectional communication. However, in scenarios with highly data-rate asymmetric links and one of the terminals severely size, weight, and power (SWaP) constrained this is not achievable [3]. Benefits have been sustained by integrating modulating retroreflectors (MRRs) [4], [5], [6] on compact platforms and transferring additional technological complexity to larger, more stationary platforms. An example is the Future Combat Air System (FCAS) in development at Airbus, where a mothership requires asymmetric communication from many remote carriers to operate cooperatively [7].

MRRs, illuminated by a continuous wave laser, directly return data encoded on to the incident beam. Semiconductor electroabsorption modulators utilizing the quantum confined Stark effect [8], encoding data by perturbation of the material absorption, have demonstrated high speed data transmission at a fraction of the power requirements of a laser [9]. These modulators are often pixelated to increase the field of view (FOV) and modulation bandwidth [6]. Subsequently to focusing of the light, only a single pixel acts on the incident beam, though an entire pixel array is powered simultaneously [10]. Large power reductions are achievable if the optically active pixel is driven in isolation. Hence enabling the capacity for an increased number of pixels, therefore enhancing the FOV without limiting the modulation bandwidth.

To reliably operate using a single pixel, it is necessary to detect an incoming signal to identify the location of the incident beam before modulating and reflecting. Typically, the quantum confined Stark effect is associated with a redshift [5], leading to a low unbiased absorption at the operating wavelength, increasing with applied electric field. While beneficial for reducing the unbiased optical losses, this is non-optimal for detection purposes.

The asymmetric or blueshifted quantum confined Stark effect, as observed in [11], [12], [13], could provide high unbiased absorption at a given wavelength – such as 1550nm for FSO applications – which can be reduced under reverse bias. Thus, a device could be operated unbiased in a photovoltaic mode until the incident signal is detected, and then be utilized for modulation maintaining low optical losses when biased.

Here, we investigated epi-structures for electroabsorption modulators, which are capable of detecting an incident beam under a zero-bias condition prior to modulation in order to reduce power consumption. This was achieved by exploiting asymmetric stepped quantum wells (ASQWs) exhibiting the asymmetric Stark effect. Full device band structure calculations were used to evaluate the shift in bound energy levels under simulated applied electric fields. The fraction of light absorbed by a single quantum well was then calculated to draw comparison between the proposed structure, a quantum well photodiode and a coupled quantum well modulator structure, from the literature composed of varied materials and geometries. Finally, thermal escape and tunneling transit times were estimated to predict responsivity. The proposed ASQW epi-structure consisting of InGaAs well, InAsP step, and GaInP barrier layers demonstrated adequate detection and enhanced modulation performance. Our findings suggest enhanced

performance at a fraction of the total onboard power consumption is achievable in MRRs for compact FSO communication. The embodiment of such a device within a FSO MRR system would operate in photovoltaic mode (all pixels unbiased) until a 1550nm signal from the mothership or base station interrogation laser was received. This signal would be used solely to activate the pixel and initiate modulation, imprinting data onto the incident beam prior to retroreflection using a back mirror and focusing optics. During single pixel modulation, all remaining pixels continue to operate in photovoltaic mode, until a signal is detected at another location. This signal would disable modulation at the initial pixel and initiate modulation at the new location. Comparing to the 36 pixels present in [14], a reduction in power consumption of up to a factor of 36 is possible, though further reduction in power consumption is scaled by the number of pixels manufactured in the array.

II. Modelling

A modelling routine consisting of band structure, absorption, and responsivity calculations was devised. The absorption component was based on calculations in [15] and [16], with comparison made to measurements reported in [6]. This was then used to calculate the quantum confined Stark effect as in [17]. Subsequently, the responsivity was evaluated and compared with the approach described in [18], following [19].

Measurements of the quantum confined Stark effect reported in [6] were conducted for a MRR. This modulator had an intrinsic region composed of 80 $In_{0.58}GaAs/In_{0.43}AlAs$ coupled quantum wells (CQWs) grown on InP, was fabricated and packaged by the Research Institutes of Sweden (RISE) [5], following a design proposed by the United States Naval Research Laboratory (NRL) in [4]. The CQW structure exhibited a typical redshifted Stark effect, and demonstrated the fastest outdoor retroreflective FSO communication link [14] making it suitable for comparison as a modulator.

Responsivity measurements and model results reported in [18] considered a photodiode with an intrinsic region composed of 30 $In_{0.53}GaAs/InP$ single quantum wells (SQWs). [18] reported a maximum responsivity of 0.5A/W at 1550nm, which made it a suitable comparison as a photodiode. The structure subsequently proposed was based on asymmetric [13], [20] and stepped [11], [12], [13] quantum wells configured to produce a blueshifted Stark effect. The CQW structure in [4], [5], [14] and the SQW structure in [18] were used for comparison as modulator and detector respectively.

A. *Band structures*

Here, full device band structures were calculated via a Schrödinger-Poisson-Current continuity equation solver, from Nextnano [21], with a single-band effective mass approximation imposed. Changes to the bound energy levels and wavefunctions under different reverse bias voltages were simulated by applying a potential difference between the p and n-cladding regions. Default material parameters from the Nextnano database were used with exception of the SQW structure, where the bandgap followed [18].

B. *Fraction of energy absorbed*

Calculated band edges, energy states and wavefunctions were read into an in-house program to calculate the absorption spectrum using the expressions derived in [15] and tabulated in [17]. For comparison of varying structures at normal incidence dependence on the thickness of the element was removed [22] to calculate the fractional change in energy through a single quantum well, γ_{well}, instead of the absorption coefficient as described in [16].

$$\gamma_{well} = \frac{4\pi\hbar}{\epsilon_0 cn(\hbar\omega)}\left(\frac{e}{2m_0}\right)^2 |M_T|^2\rho_r \times [\gamma_{ex} + \gamma_{co}](f_v - f_c) \quad (1)$$

$\hbar$ was the reduced Planck constant, ϵ_0 was the permittivity of free space, c was the speed of light in a vacuum, n was the real refractive index, $\hbar\omega$ was the energy of an incident photon, e was the unit of elementary charge, and m_0 was the electron rest mass. This term was derived from the time average of the Poynting flux [17]. $|M_T|^2$ was the transition matrix element related to the product of a term, which in normal incidence is equal to 3/2 for heavy holes and 1/2 for light holes, the bulk momentum matrix element M_b^2 - relating to the Kane energy parameter by $(m_0/6)E_p$ [23] - and the wavefunction overlap integral $|I_{ov}|^2$. ρ_r was the reduced density of states related by $1/\rho_r = \pi\hbar^2/m_r^*$, where m_r^* was the reduced effective mass, $1/m_r^* = 1/m_e^* + 1/m_h^*$. m_e^* and m_h^* were the electron and hole effective masses respectively. γ_{ex} and γ_{co} expressed contributions to the final absorbing spectrum from the bound exciton resonance in (2), and the continuum of states in (3) respectively.

$$\gamma_{ex} = \sum_n |a_0\phi(0)|^2 \frac{R_y\Gamma_b}{\left(E_{c,v} - E_B - \hbar\omega\right)^2 + {\Gamma_b}^2} \quad (2)$$

$$\gamma_{co} = \int_0^\infty \frac{dE_{cv}}{\pi} |\phi(0)|^2 \frac{\Gamma_b}{\left(E_{c,v} - \hbar\omega\right)^2 + {\Gamma_b}^2} \quad (3)$$

Excitons were modelled as individually summed Lorentzian distributions. a_0 was the exciton Bohr radius equal to $4\pi\varepsilon\hbar^2/m_r^* e^2$, with ε the static dielectric constant. $|\phi(0)|^2$ was the oscillator strength approximated by the Sommerfeld enhancement factor $s_0/[1 + \exp(-2\pi/ka_0)]$ with s_0 fitted between 2, for a quantum well (exhibiting purely 2D behavior) and 1, for bulk (exhibiting purely 3D behavior). $ka_0 = \sqrt{E_t/R_y}$, where E_t was the difference between the transition and band gap energy, decreasing in strength further from the band edge. R_y was the exciton Rydberg equal to $m_r^* e^4/2\hbar^2(4\pi\varepsilon)^2$. Γ_b was the temperature dependent half width at half maximum of the Lorentzian equal to $\Gamma_0 + \Gamma_{ph}/\exp(\hbar\omega_{LO}/k_bT)$, typically fitted to empirical absorption data [17]. Γ_0 accounted for inhomogeneous broadening mechanisms (e.g. alloy fluctuations and interface roughness scattering) which increased with applied electric field following [18], [24]. Γ_{ph} and $\hbar\omega_{LO}$ represented the coupling and energy of homogeneous broadening from longitudinal optical (LO) phonon scattering respectively. k_b was the Boltzmann constant and T was the temperature, set at 300K. $E_{c,v}$ was the interband transition energy between conduction and valence states c and v. E_B was the exciton binding energy with $E_B = -4R_y$ for 2D and $E_B = -R_y$ for 3D behavior [17]. The continuum of states contribution was modelled as a cumulatively summed Lorentzian distribution, integrated to an energy sufficiently larger than the band gap to approximate ∞. f_v and f_c were the occupation

probabilities of the corresponding conduction and valence states calculated using Fermi-Dirac statistics.

C. Responsivity

Responsivity was estimated following [18] using the calculated γ_{well}, and material parameters collated in Table 1. Two mechanisms for carrier escape from quantum wells were considered 1) thermal emission, and 2) tunneling. The time for a free carrier to transit out from the quantum well thermally was given in (4).

$$\tau_{th} = \left(\frac{2\pi m_{wi}^* L_w^2}{k_B T}\right)^{\frac{1}{2}} \exp\left(\frac{H_i}{k_B T}\right) \quad (4)$$

m_{wi}^* was the effective mass in the well, with i indexing the band (conduction, heavy hole, or light hole). L_w was the well thickness. H_i was the effective barrier height of the band i, relating to the energy difference between the barrier and the ground state energy level in the well. The time for the carrier to tunnel into the adjacent well was given by (5).

$$\tau_{tu} = \left(\frac{2m_{wi}^* L_w^2}{\pi\hbar}\right) \exp\left(\frac{2L_b\sqrt{2m_{bi}^* H_i}}{\hbar}\right) \quad (5)$$

L_b was the thickness of the barrier. m_{bi}^* was the effective mass in the barrier for a given band. The total transit time through the device was calculated in (6).

$$\tau_i = N\left(\frac{1}{\tau_{tu}} + \frac{1}{\tau_{th}}\right)^{-1} \quad (6)$$

The band with highest transit time was considered dominant and used as τ_i for the remainder of the calculation. In [18] carrier induced saturation in the absorption coefficient was calculated for high incident power. For retroreflective FSO communication an incident power of the order of 1mW was expected and therefore saturation effects were neglected. The responsivity was then calculated using (7).

$$R = \eta(1-r)\left[1 - \exp\left(-\gamma_{well}\frac{d_{abs}}{L_w}\right)\right] R_{ideal} \quad (7)$$

η was the internal quantum efficiency calculated from comparison between τ_i and the recombination lifetime, $\tau_{r,i}$ by $\tau_{r,i}/(\tau_{r,i} + \tau_i)$. r was the reflectivity of the front interface of the pixel. d_{abs} was the thickness of the active region. A ratio between d_{abs} and L_w was used to account for the inclusion of γ_{well} describing the fraction of absorbing medium within the active region. R_{ideal} was the wavelength dependent ideal responsivity equal to $q/\hbar\omega$.

D. Material selection

Observations of the asymmetric Stark effect were reported in GaAs-GaAsN stepped quantum wells in [12], type-II InP-InAsP-InGaAs stepped quantum wells in [13], and InGaAs-InP-InAsP composite quantum wells in [11], though, only [13] offered c-band operation. The type-II band alignment reduced wavefunction overlap and the absorption coefficient, reducing potential responsivity.

To utilize the asymmetric Stark effect for simultaneous c-band detection and modulation, we determined material combinations with type-I band alignment through comparison of natural valence band offsets calculated in [25]. These included binary alloy InP, and ternary alloys InGaAs, InAlAs, InAsP, and GaInP. Various combinations of barrier, step, and well material were considered to analyse the asymmetric Stark effect, an example of which is shown in Fig. 1. This was found to be driven solely by variation in the first bound state in the conduction band. The effect manifested through an apparent narrowing of the well where the first conduction state was bound, increasing confinement due to the step layer, thus increasing the separation from band edge potential.

Band structures under reverse bias were then computed to determine suitability. The following criteria were evaluated, 1) the presence of the asymmetric Stark effect, 2) a ground state transition energy within the c-band range, and 3) minimal lattice mismatch, or a potential for strain-balancing.

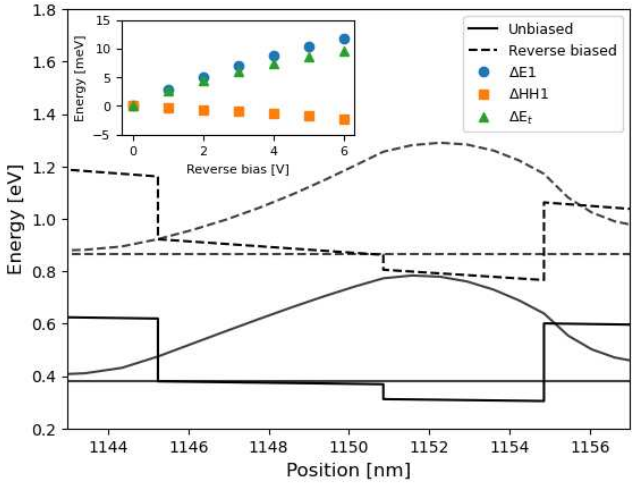

Fig. 1. – First electron wavefunction and energy level, and conduction band edge, unbiased and under reverse bias. The change in ground state electron, hole, and transition energy with applied bias is shown in the inset.

Though several material combinations met these criteria, additional considerations were given to suitability for unbiased detection. InAlAs was removed due to large barrier heights and effective masses degrading both thermal escape and tunneling transit times as described by (4) and (5). Further, growth of aluminium-based alloys could unintentionally incorporate impurities [26], such as oxygen or carbon, creating trap states which reduce the recombination lifetime, thus degrading the internal quantum efficiency. Calculations in [27] suggested that combining aluminium with GaAs reduced the recombination lifetime by an order of magnitude.

Consequently, GaInP, InAsP, and InGaAs were found to be most suitable for barrier, step, and well materials respectively. This combination provided reduced barrier heights. The asymmetric Stark effect was then established to be most pronounced (largest ground state transition energy blue shift) with a structure of 5nm $Ga_{(0.35)}InP$ – 5nm $InAs_{(0.20)}P$ – 4.5 nm $In_{(0.57)}GaAs$, where the first bound energy level in the conduction band was located proximally to the InAsP step band edge energy, similarly to that shown in Fig. 1. This formed an ASQW structure, where the step was located to assist the escaping hole. This follows examples of multiple quantum well photovoltaic device improvement using stepped barriers for enhancing internal quantum efficiency in [28], [29]. Additionally, a higher built-in potential was gained by reducing

the number of periods to 20, opposed to 30 in [18], and 80 in [4] and [5].

E. Strain-balancing

A simple calculation to estimate strain in the structure was performed similarly to [30]. First, a weighted sum of the interpolated lattice constants from [31], the shear moduli from [30], and the layer thicknesses for the barrier, step, and well materials were used to calculate the mean lattice spacing for the ASQW structure. This was compared to the substrate lattice constant of InP, giving ≈ 0.6 % mismatch. Therefore, only minimal modifications to compositions and layer thicknesses would be required during epitaxy to further reduce strain-induced defects.

F. Parameterization

TABLE I
PARAMETERS USED IN γ_{well}, RESPONSIVITY, AND QCSE CALCULATIONS

Parameter	SQW[18]	CQW[4],[5]	ASQW
Active region thickness / d_{abs} [nm]	550[18]	1528[6]	278
Barrier thickness / L_b [nm]	10[18]	6.3[6]	10
Effective masses in the well			
Electron / m_{we}^* [m_0]	0.043[31]	0.043[31]	0.047[31]
Heavy hole / m_{whh}^* [m_0]	0.37[31]	0.37[31]	0.37[31]
Light-hole / m_{wlh}^* [m_0]	0.052[31]	0.052[31]	0.058[31]
Effective masses in the barrier			
Electron / m_{be}^* [m_0]	0.08[31]	0.073[31]	0.105[31]
Heavy hole / m_{bhh}^* [m_0]	0.53[31]	0.40[31]	0.365[31]
Light-hole / m_{blh}^* [m_0]	0.12[31]	0.11[31]	0.17[31]
Inhomogeneous broadening energy / Γ_0 [meV]	6.0[32]	6.0[17]	6.0[17]
Kane energy Parameter / E_p [eV]	25.3[31]	25.3[31]	26.0[31]
LO-phonon energy / $\hbar\omega_{LO}$ [meV]	30[32]	35[17]	35[17]
LO-phonon coupling energy / Γ_{ph} [meV]	15.3[17]	15.3[17]	15.3[17]
Number of periods	30[18]	80[6]	20
Recombination lifetime / τ_{rec} [ns]	1500[18]	1[27]	10[33]
Reflectivity / r	0.1	0.1	0.1
Refractive index / n_r	3.38[34]	3.38[34]	3.38
Static dielectric constant / ϵ	13.9[32]	13.9[32]	13.9
Well thickness / L_w [nm]	8.0[18]	12.8[6]	4.5

The parameters in Table 1 were used in γ_{well} and responsivity calculations. Material parameters were taken from [31] unless otherwise specified. The inhomogeneous broadening energy was set to 6 meV as suggested for InGaAs lattice matched to InP in [17], [32]. Similarly, the LO-phonon energy and coupling were set according to [17], [32]. Although these values require experimental verification, they were a suitable approximation considering the similarity of the materials defined. The reflectivity at the front surface was set to 0.1 assuming anti-reflection coating was applied as in FSO applications.

η, and hence responsivity, R, were highly sensitive to $\tau_{r,i}$, which had high uncertainty and was used as a fitting parameter in external quantum efficiency studies [35]. $\tau_{r,i}$ is directly proportional to temperature [36], inversely proportional to wavefunction overlap [37], and observed to be larger with the removal of aluminimum based alloys [26], [27]. Though these considerations were expected to increase $\tau_{r,i}$ in ASQW structures there was a large range of values from 0.1ns-1.5µs reported for varying structures in [18], [33], [35]. Therefore an estimate of 10ns was assumed following [33], but minimum and maximum values of responsivity were subsequently calculated. Accordingly, characterization following epitaxy would be required to determine and then optimize these parameters in future studies.

III. RESULTS

The SQW band structure, applied as a photodiode in [18], is shown in Fig. 2. The CQW band structure, applied as a MRR in [4] and [5], is shown in Fig. 3. The ASQW band structure reported here is shown in Fig. 4. Full device band structures, including cladding regions were calculated, though only the central period is shown in Fig. 2-4. The calculated ground and first excited state energy levels are shown for the conduction band E_c and the heavy hole valence band E_{hh}. Only the ground state energy level and wavefunction for the light hole valence band E_{lh} is shown as the higher energy excited state does not significantly contribute to absorption at the band edge.

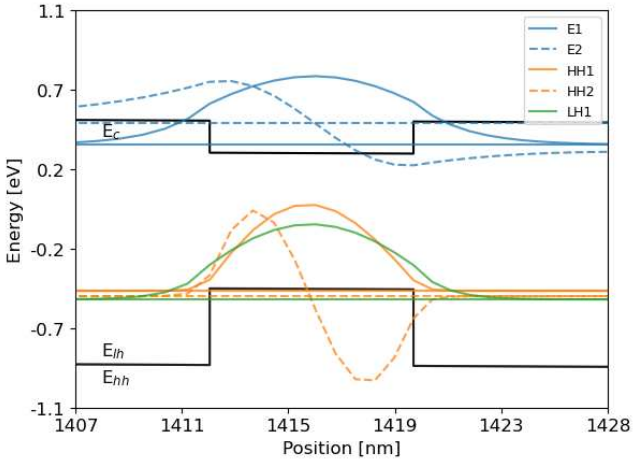

Fig. 2. – SQW [18] band structure, bound energy states and wavefunctions.

The SQW in Fig. 2 showed high symmetry and wavefunction overlap suggestive of a lower recombination lifetime under zero bias as reflected by the measurements in [18]. However, this will also increase absorption and hence internal quantum efficiency. We observe wavefunction asymmetry even when unbiased in the CQW in Fig. 3. Under reverse bias forbidden transitions become more apparent as in [38] which is suggested to offer a strong Stark effect [39]. The CQW has the largest effective width and therefore closely spaced energy levels in both conduction and valence bands.

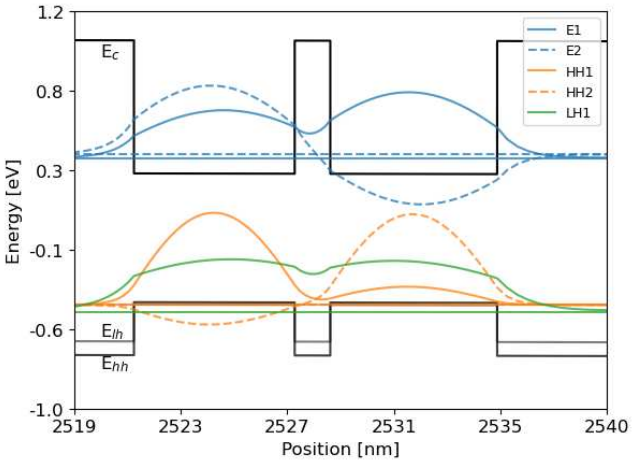

Fig. 3. – CQW [4], [5] band structure, bound energy states and wavefunctions.

The SQW in Fig. 2 and the ASQW in Fig. 4 show greater barrier height in the valence band, suggesting recombination is limited by holes. The wavefunction overlap is lower in the ASQW, which reduces the overall absorption magnitude, but may have benefits for detection through increased recombination lifetime [37], and for modulation through reduced insertion loss. The height of the step in the ASQW valence band is 43meV lower than the barrier in the SQW structure, which may also assist thermal escape [28], [29].

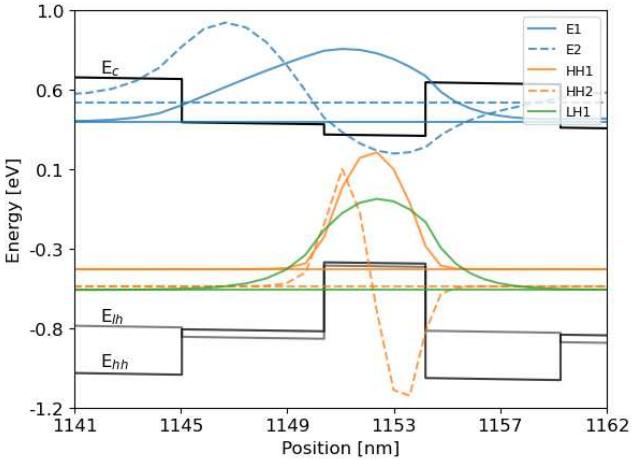

Fig. 4. – ASQW band structure, bound energy states and wavefunctions.

Γ_{well} for each structure when unbiased, is shown in Fig. 5 with the highest in the CQW due to overlapping contributions from both the continuum of states and closely spaced excitons. The ASQW γ_{well} has significantly fewer contributions due to the higher confinement, and larger energy separation to the excited states in the 4.5nm quantum well, which is particularly pronounced for the valence states. The modelled effect of an applied electric field on γ_{well} is shown for CQW and ASQW as a comparison of modulator performance in fig. 6 and 7. This was calculated at 0, 3, and 6V reverse bias, although due to the thickness of the intrinsic region the electric field strength was higher in the ASQW.

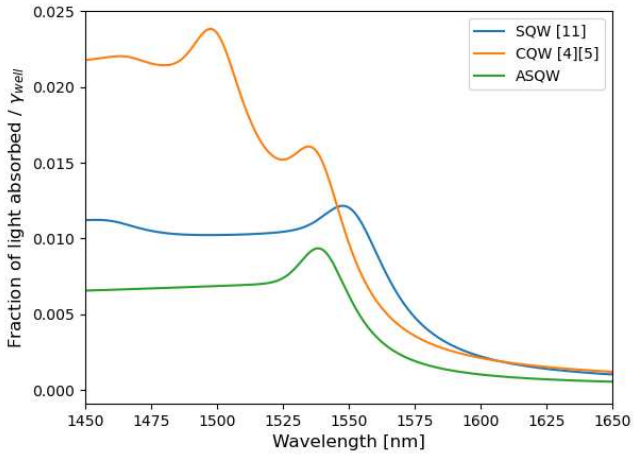

Fig. 5. – γ_{well} calculated for structures from SQW [18], CQW [4], [5], and ASQW.

The extinction ratio (ER) is shown in the inset calculated as ER = $10\log_{10}(\gamma_{well,ON} / \gamma_{well,OFF})$ where $\gamma_{well,ON}$ and $\gamma_{well,OFF}$ represent the fraction of light absorbed when the device is operated for maximum and minimum transmission respectively. The predicted γ_{well} for the CQW structure shows the same features as the measured absorption spectra reported in [4] and [5], with the ER closely matching the experimental value in [6] under 6V. We observe a sharp decrease in γ_{well} at 1550nm due to the redshift and reduction in wavefunction overlap of the ground state transition with reverse bias. This is accompanied by an increasing wavefunction overlap between first electron and second heavy hole (E1-HH2) states, which coincides with the redshift of the first electron and light hole (E1-LH1) transition. The E1-HH2 and E1-LH1 absorption contributions occur at a similar wavelength enhancing the Stark effect as in [39].

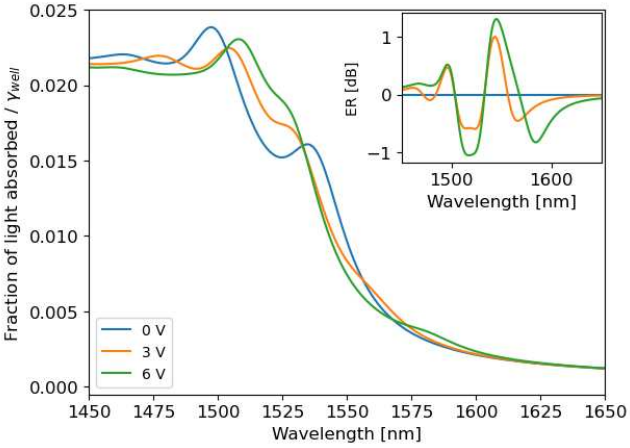

Fig. 6. - γ_{well} unbiased and under 3 and 6 V reverse bias for CQW structure. ER is shown inset.

The change in γ_{well} for the ASQW in Fig. 7 displays a strong asymmetric Stark effect similarly to [12], with energy blueshift and an increase in the wavefunction overlap with reverse bias. Though the magnitude of γ_{well} is lower in the ASQW, a significant ER is predicted over a broader wavelength range than for the CQW. The 6V ERs for the CQW and ASQW structures are compared in Fig. 8.

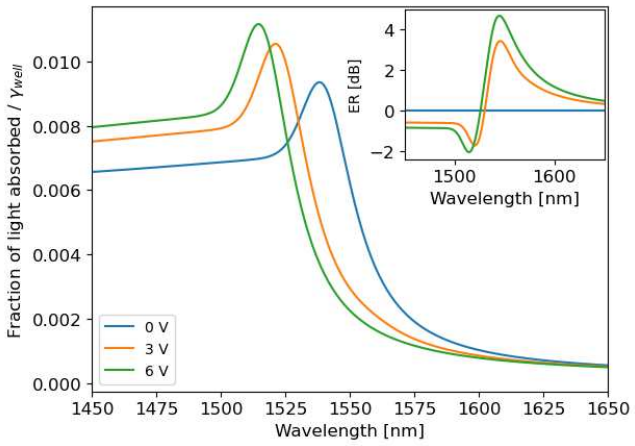

Fig. 7. - γ_{well} unbiased and under 3 and 6 V reverse bias for ASQW structure. ER is shown inset.

At an equivalent voltage there is an enhancement in the ER of the ASQW, which can be partially attributed to the strength of the asymmetric Stark shift. The reduced intrinsic thickness in the ASQW, to improve carrier transit for detection, has a higher electric field across the quantum wells. The calculated electric field strengths at 6V are ≈ 65 kV/cm in the CQW and ≈ 113 kV/cm in the ASQW. Nevertheless, under 3V, the ASQW exhibits an ER almost three times greater than the CQW under 6V, with a comparable electric field strength of ≈ 67 kV/cm.

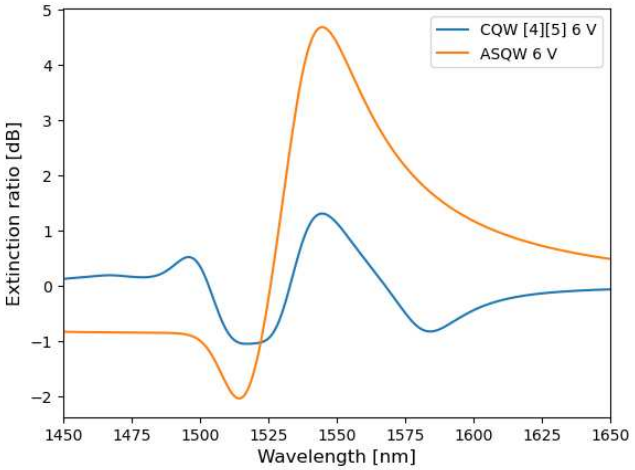

Fig. 8. – ER for a 6V reverse bias swing for CQW and ASQW structures.

The responsivity is shown in Fig. 9 with a logarithmic y-axis to reflect the large disparity between recombination lifetimes and hence internal quantum efficiencies. Though the ASQW is less favourable solely as a detector than the SQW it provides a responsivity large enough to exceed the expected dark current and therefore could be used for detection only to initialise modulation.

The SQW modelled and measured in [18] has a recombination lifetime two orders of magnitude larger than the ASQW. The measurements of responsivity in [18] fitted with recombination lifetime of 1.5μs indicate the quality of the material growth of the wafer. The recombination lifetime values prescribed to the CQW and the ASQW assume a higher defect density in these structures, particularly for the aluminium-based barrier materials in the CQW. Therefore, growth and characterization of the ASQW may yield even higher responsivity.

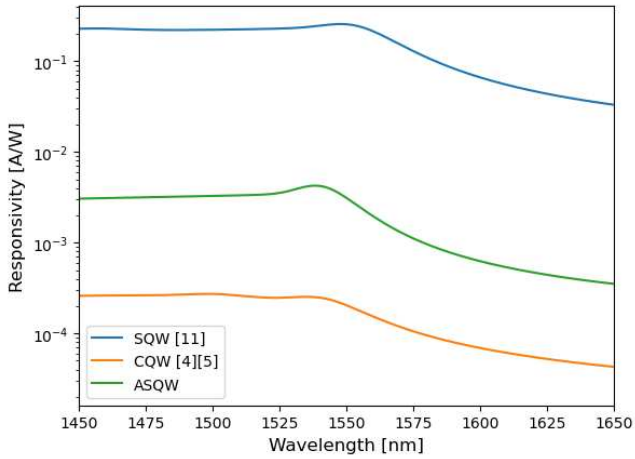

Fig. 9. – Responsivity calculated for SQW, CQW, and ASQW structures.

The responsivity, and photocurrent at 1mW incident power, for the ASQW is shown in Fig. 10. An incident power typical of a received FSO signal was used. From Fig. 10 a maximum responsivity of 0.004 A/W and a maximum photocurrent of 4μA is predicted, which is up to three orders of magnitude greater than predicted dark current and will allow for photovoltaic signal detection to enable modulation. A 20% uncertainty in the recombination lifetime has been included in Fig. 10 to illustrate the sensitivity to this parameter.

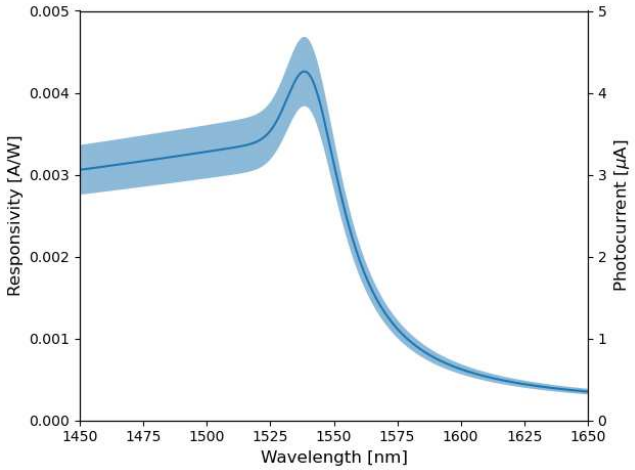

Fig. 10. – Responsivity, and photocurrent at 1mW incident laser power, for the ASQW structure. Shaded area indicates +/– 20% uncertainty in the recombination lifetime.

IV. Discussion

As modulation is the primary application of the ASQW, Table 2 shows performance metrics of MQW-EAMs used as MRRs in FSO data links, with the requirements as a detector discussed subsequently. Table 2 suggests improvements in data-rate tend to correspond to increases in power consumption (P) and IL, with decreases in FOV and ER. Though the ASQW has a reduced active layer thickness needed to reduce carrier transit

time, reducing the theoretical maximum modulation bandwidth, utilising unbiased detection with only a single pixel modulating at any time, power consumption is significantly reduced.

TABLE II
LITERATURE 1550NM FSO-MRR MQW-EAM PERFORMANCE

Year	Data-rate (Mb/s)	FOV (°)	ER (dB)	IL (dB)	P (W)	Ref
2004	70	20	3	-	3	[40]
2007	45	10	3	0.7	-	[41]
2021	500	6.4	2	11.5	8	[14]

Moreover, by reducing the power consumption we enable the manufacture of larger pixel arrays and are able to further increase the FOV. Though this design has benefits for reductions in power consumption and improvements in FOV, other metrics for application to a full FSO system must be considered. The data-rate will be impacted by the large reduction in the active layer thickness, increasing the capacitance and reducing the modulation bandwidth. As the bandwidth is proportional to active layer thickness, assuming the same pixel area and resistance, the bandwidth of the ASQW may be a factor of 4 less than the CQW. Nevertheless, the significant enhancement in ER, a factor of two greater than shown in Table 2, may offset this if operated under a reduced bias swing, while still maintaining a higher ER resulting in a lower reduction of device data-rate. Additionally, the reduction in active layer thickness and the fraction of light absorbed also reduces the insertion loss of the device, which is beneficial for long distance data links.

The responsivity and photocurrent reported here is nominally low relative to other examples of experimental multiple quantum well photodiode or photovoltaic devices [28], [29], [42], which are of the same order of magnitude as the 0.3 A/W reported in [18]. However, in comparison to dark current values in the low nA range [42], [43], [44], particularly when unbiased, the ASQW offers appropriate photocurrent generation to distinguish from background noise. Further, considerations have been taken to reduce sources of dark current, such as removing the aluminum-based alloys from our design [26], [27] and reducing the intrinsic region thickness [43], [45]. As mentioned previously, the responsivity is highly sensitive to the recombination lifetime, with values spanning the range of 0.1ns-1.5μs [18], [33], [35]. Therefore, we note that with a 0.1ns recombination lifetime a photocurrent of 40nA was predicted, which will dramatically lower the signal to noise ratio if dark current is particularly high, and reduce the efficacy of the device. Nevertheless, if high quality material growth is achieved, and hence recombination lifetimes of the order 100ns or even 1μs, it may even be possible to integrate energy harvesting capabilities with MRRs, utilizing simultaneous wireless information and power transfer [46]. Ultimately, high quality growth followed by optimization (particularly applying correct strain offsetting) will be essential in final devices.

The predicted quantum confined Stark effect suggests improved modulator performance in comparison to the CQW structure, both at equivalent reverse bias voltages and electric field strengths. Yet, due to the reduction in the intrinsic region thickness and absorption magnitude, it may be necessary to increase the number of periods to impart a higher level of modulation on the incident beam. Though, the reduced absorption will undoubtedly offer benefits in long distance retroreflective FSO data links by reducing the insertion loss.

By integrating detection and modulation capabilities on a single pixel, large reductions in the onboard power requirements are achievable, either enhancing the SWaP budget onboard compact platforms (such as drones and satellites) for inclusion of additional functionality or further minimizing the total SWaP requirements for these devices. This design eliminates the relation between power consumption and the number of pixels in the modulating array, thereby removing limitation on the total pixel quantity. Provided arrays containing higher pixel quantities can be fabricated with suitable yield, larger area devices with significantly increased fields of view are achievable.

V. CONCLUSION

A modelling procedure including calculations for full device band structures, fraction of light absorbed in quantum wells, and responsivity was described. An asymmetric stepped quantum well structure composed of a 20 period intrinsic region was proposed as a device for both detecting and modulating incident light for application to MRRs for FSO communication data links. Each period contained a 5nm $Ga_{(0.35)}InP$ barrier, 5nm $InAs_{(0.20)}P$ step, and 4.5nm $In_{(0.57)}GaAs$ well. This exhibited a strong asymmetric Stark effect: blueshift and increase in wavefunction overlap for the ground state transition. This was predicted to enhance the extinction ratio from the previous coupled quantum well design by up to a factor of 4. Finally, a responsivity of 0.004, corresponding to a photocurrent of 4μA at 1mW incident laser power, was predicted. This offers large enough photocurrent generation to detect an incident signal when unbiased and then trigger modulation requiring only one of thirty-six pixels, in the current design, to be active at any one time. This will have significant implications on the overall power consumption of retroreflective FSO devices. If higher recombination lifetimes can be achieved energy harvesting may be possible to further reduce power constraints onboard compact platforms and incorporate simultaneous wireless information and power transfer.

ACKNOWLEDGEMENTS

This research was funded by the Future Compound Semiconductor Manufacturing Hub through UKRI grant EP/P006973/1. For the purpose of open access, the author has applied a Creative Commons Attribution (CC BY) license to any Author Accepted Manuscript version arising.

DATA-ACCESS STATEMENT

Data underpinning the research presented in this article can be found in the Cardiff University Data Catalog at http://doi.org/10.17035/d.2024.0310602816.

REFERENCES

[1] H. Willebrand and B. Ghuman, *Free Space Optics: Enabling Optical Connectivity in Today's Networks*. USA: Sams, 2001.

[2] M. A. Khalighi and M. Uysal, "Survey on Free Space Optical Communication: A Communication Theory Perspective," *IEEE Communications Surveys & Tutorials*, vol. 16, no. 4, pp. 2231–2258, 2014, doi: 10.1109/COMST.2014.2329501.

[3] G. C. Gilbreath, "Progress in development of multiple-quantum-well retromodulators for free-space data links," *Opt. Eng*, vol. 42, no. 6, p. 1611, Jun. 2003, doi: 10.1117/1.1572155.

[4] T. H. Stievater, W. S. Rabinovich, P. G. Goetz, R. Mahon, and S. C. Binari, "A Surface-Normal Coupled-Quantum-Well Modulator at 1.55<tex>mu</tex>m," *IEEE Photonics Technology Letters*, vol. 16, no. 9, pp. 2036–2038, Sep. 2004, doi: 10.1109/LPT.2004.831981.

[5] Q. Wang, B. Noharet, S. Junique, S. Almqvist, D. Ågren, and J. Y. Andersson, "1550 nm transmissive/reflective surface-normal electroabsorption modulator arrays," *Electron. Lett.*, vol. 42, no. 1, p. 47, 2006, doi: 10.1049/el:20063504.

[6] C. Quintana *et al.*, "High Speed Electro-Absorption Modulator for Long Range Retroreflective Free Space Optics," *IEEE Photonics Technology Letters*, vol. 29, no. 9, pp. 707–710, May 2017, doi: 10.1109/LPT.2017.2680842.

[7] "https://www.airbus.com/en/products-services/defence/multi-domain-superiority/future-combat-air-system-fcas."

[8] D. A. B. Miller *et al.*, "Band-Edge Electroabsorption in Quantum Well Structures: The Quantum-Confined Stark Effect," *Phys. Rev. Lett.*, vol. 53, no. 22, pp. 2173–2176, Nov. 1984, doi: 10.1103/PhysRevLett.53.2173.

[9] W. S. Rabinovich *et al.*, "Free-space optical communications research and demonstrations at the US Naval Research Laboratory," *Applied Optics*, vol. 54, no. 31, p. F189, Nov. 2015, doi: 10.1364/AO.54.00F189.

[10] P. G. Goetz *et al.*, "Multiple quantum well-based modulating retroreflectors for inter- and intra-spacecraft communication," in *Photonics for Space Environments XI*, E. W. Taylor, Ed., SPIE, 2006, p. 63080A. doi: 10.1117/12.694907.

[11] B. Aneeshkumar, A. Yu. Silov, M. R. Leys, and J. H. Wolter, "Large asymmetric Stark shift in GaxIn1−xAs/InP/InAsyP1−y composite quantum wells," *Appl. Phys. Lett.*, vol. 83, no. 14, pp. 2838–2840, Oct. 2003, doi: 10.1063/1.1616664.

[12] A. C. H. Lim, R. Gupta, S. K. Haywood, M. J. Steer, M. Hopkinson, and G. Hill, "Electric field induced blueshift of the e1-hh1 exciton transition in a GaAs1−xNx/GaAs (x<1%) stepped quantum well," *Appl. Phys. Lett.*, vol. 89, no. 26, p. 261110, Dec. 2006, doi: 10.1063/1.2424278.

[13] S. K. Haywood *et al.*, "Demonstration of a blueshift in type II asymmetric InP/InAsP/InGaAs multiple quantum wells," *Journal of Applied Physics*, vol. 94, no. 5, pp. 3222–3228, Sep. 2003, doi: 10.1063/1.1598639.

[14] C. Quintana *et al.*, "A High Speed Retro-Reflective Free Space Optics Links With UAV," *J. Lightwave Technol.*, vol. 39, no. 18, pp. 5699–5705, Sep. 2021, doi: 10.1109/JLT.2021.3091991.

[15] S.-L. Chuang, S. Schmitt-Rink, D. A. B. Miller, and D. S. Chemla, "Exciton Green's-function approach to optical absorption in a quantum well with an applied electric field," *Physical Review B*, vol. 43, no. 2, pp. 1500–1509, Jan. 1991, doi: 10.1103/PhysRevB.43.1500.

[16] P. Blood, *Quantum confined laser devices: optical gain and recombination in semiconductors*, First edition. in Oxford master series in physics. Atomic, optical, and laser physics, no. 23. Oxford: Oxford University Press, 2015.

[17] S. L. Chuang, "Physics of Photonic Devices," p. 841, 2009.

[18] G. Zhou and P. Runge, "Modeling of Multiple-Quantum-Well p-i-n Photodiodes," *IEEE J. Quantum Electron.*, vol. 50, no. 4, pp. 220–227, Apr. 2014, doi: 10.1109/JQE.2014.2305015.

[19] A. M. Fox, D. A. B. Miller, G. Livescu, J. E. Cunningham, and W. Y. Jan, "Quantum well carrier sweep out: relation to electroabsorption and exciton saturation," *IEEE Journal of Quantum Electronics*, vol. 27, no. 10, pp. 2281–2295, 1991, doi: 10.1109/3.97272.

[20] R. K. Gug and W. E. Hagston, "Large blue shifts induced by the quantum confined stark effect in asymmetric quantum wells," *Appl. Phys. Lett.*, vol. 73, no. 11, pp. 1547–1549, Sep. 1998, doi: 10.1063/1.122201.

[21] S. Birner *et al.*, "nextnano: General Purpose 3-D Simulations," *IEEE Transactions on Electron Devices*, vol. 54, no. 9, pp. 2137–2142, Sep. 2007, doi: 10.1109/TED.2007.902871.

[22] P. Blood, "On the dimensionality of optical absorption, gain, and recombination in quantum-confined structures," *IEEE J. Quantum Electron.*, vol. 36, no. 3, pp. 354–362, Mar. 2000, doi: 10.1109/3.825883.

[23] E. O. Kane, "Band structure of indium antimonide," *Journal of Physics and Chemistry of Solids*, vol. 1, no. 4, pp. 249–261, Jan. 1957.

[24] P. J. Stevens, M. Whitehead, G. Parry, and K. Woodbridge, "Computer modeling of the electric field dependent absorption spectrum of multiple quantum well material," *IEEE Journal of Quantum Electronics*, vol. 24, no. 10, pp. 2007–2016, Oct. 1988, doi: 10.1109/3.8536.

[25] S.-H. Wei and A. Zunger, "Calculated natural band offsets of all II–VI and III–V semiconductors: Chemical trends and the role of cation *d* orbitals," *Appl. Phys. Lett.*, vol. 72, no. 16, pp. 2011–2013, Apr. 1998, doi: 10.1063/1.121249.

[26] B. L. Smith *et al.*, "Characterization of InAlAs solar cells grown by MOVPE," in *2014 IEEE 40th Photovoltaic Specialist Conference (PVSC)*, Denver, CO, USA: IEEE, Jun. 2014, pp. 1180–1185. doi: 10.1109/PVSC.2014.6925125.

[27] K. Barnham *et al.*, "Quantum well solar cells," *Applied Surface Science*, vol. 113–114, pp. 722–733, 1997, doi: https://doi.org/10.1016/S0169-4332(96)00876-8.

[28] Y. Wen, Y. Wang, K. Watanabe, M. Sugiyama, and Y. Nakano, "Effect of GaAs step layer thickness in InGaAs/GaAsP stepped quantum-well solar cell," in *2012 IEEE 38th Photovoltaic Specialists Conference (PVSC) PART 2*, Austin, TX, USA: IEEE, Jun. 2012, pp. 1–6. doi: 10.1109/PVSC-Vol2.2012.6656795.

[29] Y. Wen, Y. Wang, M. Sugiyama, and Y. Nakano, "Evidence for enhanced carrier escape from multiple stepped quantum well (MSQW) and its impact on photovoltaic performance".

[30] C. G. Van de Walle, "Band lineups and deformation potentials in the model-solid theory," *Physical Review B*, vol. 39, no. 3, 1989.

[31] I. Vurgaftman, J. R. Meyer, and L. R. Ram-Mohan, "Band parameters for III–V compound semiconductors and their alloys," *Journal of Applied Physics*, vol. 89, no. 11, pp. 5815–5875, Jun. 2001, doi: 10.1063/1.1368156.

[32] M. Sugawara, T. Fujii, S. Yamazaki, and K. Nakajima, "Theoretical and experimental study of the optical-absorption spectrum of exciton resonance in In 0.53 Ga 0.47 As/InP quantum wells," *Phys. Rev. B*, vol. 42, no. 15, pp. 9587–9597, Nov. 1990, doi: 10.1103/PhysRevB.42.9587.

[33] S. Kotamraju, M. Sukeerthi, and S. E. Puthanveettil, "Modeling of InGaP/InGaAs-GaAsP/Ge multiple quantum well solar cell to improve efficiency for space applications," *Solar Energy*, vol. 186, pp. 328–334, Jul. 2019, doi: 10.1016/j.solener.2019.05.015.

[34] H. W. Dinges, H. Burkhard, R. Lösch, H. Nickel, and W. Schlapp, "Refractive indices of InAlAs and InGaAs/InP from 250 to 1900 nm determined by spectroscopic ellipsometry," *Applied Surface Science*, vol. 54, pp. 477–481, Jan. 1992, doi: 10.1016/0169-4332(92)90090-K.

[35] G. K. Bradshaw, C. Z. Carlin, J. P. Samberg, P. C. Colter, and S. M. Bedair, "Determination of carrier recombination lifetime in InGaAs quantum wells from external quantum efficiency measurements," in *2013 IEEE 39th Photovoltaic Specialists Conference (PVSC)*, Tampa, FL, USA: IEEE, Jun. 2013, pp. 0264–0267. doi: 10.1109/PVSC.2013.6744143.

[36] J. Nelson, M. Paxman, K. W. J. Barnham, J. S. Roberts, and C. Button, "Steady-state carrier escape from single quantum wells," *IEEE J. Quantum Electron.*, vol. 29, no. 6, pp. 1460–1468, Jun. 1993, doi: 10.1109/3.234396.

[37] R. Schwedler, H. Mikkelsen, K. Wolter, D. Laschet, J. Hergeth, and H. Kurz, "InGaAs/InP multiple quantum well modulators in experiment and theory," *J. Phys. III France*, vol. 4, no. 12, pp. 2341–2359, Dec. 1994, doi: 10.1051/jp3:1994281.

[38] M. K. Chin, "Modeling of InGaAs/InAlAs coupled double quantum wells," *Journal of Applied Physics*, vol. 76, no. 1, pp. 518–523, Jul. 1994, doi: 10.1063/1.357104.

[39] S. R. Andrews, C. M. Murray, R. A. Davies, and T. M. Kerr, "Stark effect in strongly coupled quantum wells," *Physical Review B*, vol. 37, no. 14, pp. 8198–8204, May 1988, doi: 10.1103/PhysRevB.37.8198.

[40] W. S. Rabinovich *et al.*, "Performance of cat's eye modulating retroreflectors for free-space optical communications," in *Free-Space Laser Communications IV*, SPIE, 2004, pp. 104–114.

[41] W. S. Rabinovich *et al.*, "45-Mbit/s cat's-eye modulating retroreflectors," *Optical Engineering*, vol. 46, no. 10, pp. 104001–104001, 2007.
[42] C. I. Cabrera, J. C. Rimada, J. P. Connolly, and L. Hernandez, "Modelling of GaAsP/InGaAs/GaAs strain-balanced multiple-quantum well solar cells," *Journal of Applied Physics*, vol. 113, no. 2, p. 024512, Jan. 2013, doi: 10.1063/1.4775404.
[43] D. B. Bushnell *et al.*, "Effect of barrier composition and well number on the dark current of quantum well solar cells".
[44] B. Tossoun *et al.*, "High-Speed InP-Based p-i-n Photodiodes With InGaAs/GaAsSb Type-II Quantum Wells," *IEEE Photon. Technol. Lett.*, vol. 30, no. 4, pp. 399–402, Feb. 2018, doi: 10.1109/LPT.2018.2793663.
[45] A. Freundlich, M. F. Vilela, P. Renaud, C. Monier, and A. Delaney, "InAsP/InP Multi Quantum Well Solar Cells: An improved design for high radiation orbit operation," in *Space technology and applications international forum (STAIF - 97)*, Albuquerque, New Mexico (USA): ASCE, 1997, pp. 881–886. doi: 10.1063/1.52095.
[46] Y. Bai, Q. Liu, R. Chen, Q. Zhang, and W. Wang, "Long-Range Optical Wireless Information and Power Transfer." arXiv, Jul. 06, 2022. Accessed: Mar. 02, 2023. [Online]. Available: http://arxiv.org/abs/2108.00004

Benjamin C. Maglio received the Ph.D. degree in physics from Cardiff University, Cardiff, U.K. in 2022 studying quantum well and dot modulators and lasers for free space and on-chip optical communication. Subsequently he worked as a Research Associate in the Optoelectronics Group at Cardiff University. Since 2023, he has been a Postdoctoral Fellow with the University of Alaska Fairbanks, Institute of Arctic Biology, Fairbanks, AK, United States. His current research topics include free space optical quantum well devices, doped quantum dot laser diodes for photonic integrated circuits, as well as modeling carbon and methane fluxes in terrestrial wetland ecosystems.

Crisanto Quintana received the Ph.D. degree in electrical engineering from University of Las Palmas de Gran Canaria, Spain, in 2012. His thesis dealt with the use of time hopping spread techniques in free space optical systems. From 2013-2018 he joined University of Oxford to conduct research in the field of retroreflective free space optics. In 2018 he joined Airbus Operations as a research scientist where he has been working on low, size, weight and power free space optical terminals.

Yoann Thueux, is currently a Research Project Leader at Airbus receiving the MSc degree in Communication Systems & Signal Processing from the University of Bristol in 2001. Subsequently, he worked as a Research, Senior, and Principal Scientist at BAE Systems before joining Airbus, where he has led projects in computer vision, laser communications and power beaming.

Peter M. Smowton (Senior Member, IEEE), Professor Peter Smowton directs the EPSRC Future Compound Semiconductor Manufacturing Hub and the EPSRC Centre for Doctoral Training in Compound Semiconductor Manufacturing and is the Managing Director of the Institute for Compound Semiconductors at Cardiff University. He is active in the South Wales Compound Semiconductor Cluster and has published over 200 papers focused on the physics of optoelectronic devices and their manufacture.